Mar Geophys Res (2014) 35:21–35
DOI 10.1007/s11001-013-9203-7

ORIGINAL RESEARCH PAPER

Canyon-infilling and gas hydrate occurrences in the frontal fold of the offshore accretionary wedge off southern Taiwan

Che-Chuan Lin · Andrew Tien-Shun Lin · Char-Shine Liu · Chorng-Shern Horng · Guan-Yu Chen · Yunshuen Wang

Received: 14 April 2013 / Accepted: 15 October 2013 / Published online: 26 October 2013

Abstract We utilized reflection seismic and bathymetric data to infer the canyon-infilling, fold uplift, and gas hydrate occurrences beneath the frontal fold at the toe of the accretionary wedge, offshore SW Taiwan. The lateral migrating paleo-Penghu canyons has cut across the frontal fold with six distinct canyon/channel incisions marked by channel infills. The longitudinal bathymetric profile along the modern canyon course shows a knickpoint of ~300 m relief at this frontal fold, indicating that the rate of fold uplift is greater than that of canyon incision. The age for the initial thrusting of this fontal fold is around 240 kyr ago, as estimated by using the maximum thickness of growth strata of this fold divided by the sedimentation rate obtained from a nearby giant piston core. Bottom simulating reflector (BSR) on seismic sections indicates the base of gas hydrate stability zone. Beneath the frontal fold, there is a widespread occurrence of BSRs, suggesting the highly probable existence of substantial quantities of gas hydrates. A seismic flat spot and a few push-down reflectors below BSR are found lying beneath the anticlinal axis with bathymetric four-way dip closure. The flat spot, cutting across a series of dipping reflections beneath BSR, may indicate the contact between free gas and its underlying formation water. The push-down reflectors beneath BSRs are interpreted to result from abundant free gas hosted beneath the gas hydrate stability zone. The multiple paleo-canyon infills seen along and beneath the frontal fold and above BSRs may provide thick porous sands to host gas hydrates in the frontal fold.

Keywords Accretionary wedge · Frontal front · Submarine canyon · Gas hydrate

C.-C. Lin · A. T.-S. Lin (✉) · G.-Y. Chen
Department of Earth Sciences, National Central University, No.300, Jhongda Rd., Jhongli City 32001, Taoyuan County, Taiwan
e-mail: andrewl@ncu.edu.tw

C.-C. Lin · C.-S. Liu
Institute of Oceanography, National Taiwan University, No. 1, Sec. 4, Roosevelt Road, Taipei 10617, Taiwan

C.-S. Horng
Institute of Earth Sciences, Academia Sinica, No. 128, Sec. 2, Academia Road, Nankang, Taipei 115, Taiwan

Y. Wang
Central Geological Survey, MOEA, No. 2, Ln. 109, Huaxin St., Zhonghe Dist., New Taipei City 235, Taiwan

Introduction

An accretionary wedge forms on a non-subducting tectonic plate and consists of offscrapped sediments from the subducting plate in a convergent plate boundary (see Cawood et al. 2009 for a review). The off scrapped sediments lie over an arc ward-dipping decollement surface or a plate interface and consist of a series of folds and thrust slices such as the case in the Nankai accretionary prism (e.g., Moore et al. 2001). The accreted sediments are riddled with faults, fractures and dipping porous beds. All the above geological entities may serve as good fluid conduits that tap upward migrating gas-charged fluids (e.g., Tobin and Saffer 2009). The frontal fold (or first fold) locates at the toe of the accretionary wedge and at the end of a dipping decollement surface, a major fluid conduit in accretionary wedges (Minshull and White 1989; Shipley et al. 1994). Naturally, the frontal fold is likely to serve as a terminal structural trap for deep-seated hydrocarbons/fluids charging especially through the decollement surface. Cooper

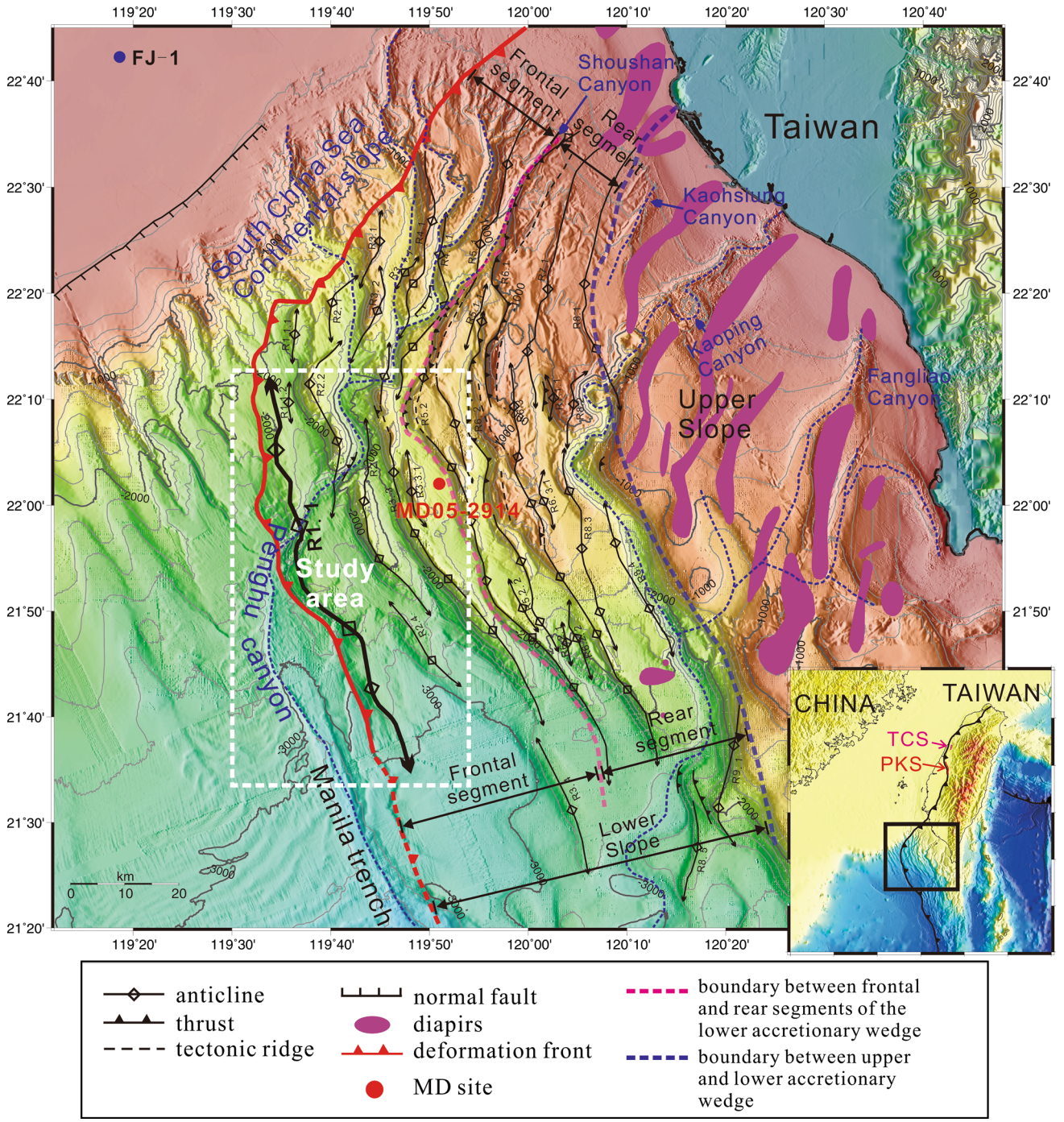

Fig. 1 Topographic and tectonic features offshore SW Taiwan. The *white rectangle* marks the study area. The well, FJ-1, in the shelf is used to derived the sediment velocity function for the study area. The structure names (R1.1–R9.1) are after Lin et al. (2008). The *red filled circle* shows the location of MD05-2914 which is used to estimate the sedimentation rate in the study area. PKS and TCS in the index map are two frontal structures onshore Taiwan

(2007) pointed out that the most hydrocarbon-prospective area of a fold-and-thrust belt is the external foothill belt between the leading thrust of the internal zone and the limit of thrusting in the foreland basin, whether emergent or buried. As a result, there is a stronger possibility of the frontal thrust creating a giant field than for structures that are further back from the thrust front (Cooper 2007). In the onshore fold-and-thrust belt of Taiwan, an active frontal fold in NW Taiwan, the Tiechanshan anticline (TCS in the inset figure of Fig. 1), hosts the largest natural gas reserve (around 1 trillion cubic feet, Yang et al. 1994) in Taiwan. This field testifies that a frontal fold may accumulate a

substantial quantity of hydrocarbon under favorable conditions.

The frontal fold (or first fold) juxtaposed to the deformation front is the youngest and active anticlinal ridge of orogenic (or accretionary) wedge offshore SW Taiwan (Fig. 1). The deformation front is not only an important tectonic boundary between the compressive orogenic wedge and the adjacent rifted South China Sea continental margin, but also a major structural trap that may host a significant amount of gas at the end and above the arcward-dipping decollement surface of the orogenic wedge. Offshore SW Taiwan, there is a few canyons cutting along and across the accretionary wedge. The Penghu canyon is one of those canyons, delivering Taiwan and China-derived coarse sediments (especially during lowered sea levels) into the abyssal South China Sea (Chuang and Yu 2002). The main courses of the recent Penghu submarine canyon have cut across the middle part of the frontal fold and a few distinct U- or V-shaped canyon incisions and subsequent canyon-infills are seen beneath the frontal fold. Since the Penghu canyon is a major sediment conduit for sediment gravity flows it is reasonable to speculate that some of the canyon-infills may be sand prone, serving as good gas hydrate reservoirs.

Previous studies have revealed tectonic features of the accretionary wedge off SW Taiwan using seismic images (Reed et al. 1992; Liu et al. 1997; Lin et al. 2008, 2009a) whilst the detail sedimentary and structural features of this frontal fold are not given. Though the very likely occurrences of gas hydrates offshore SW Taiwan have also been reported in many studies (e.g., Chi et al. 2006; Liu et al. 2006; Lin et al. 2009b; Wang et al. 2009), those studies do not specifically discuss the gas hydrate occurrences and canyon-fillings in the frontal fold. Therefore it is desirable to characterize the gas hydrate occurrences, canyon-infilling, and the structural features for the frontal fold off SW Taiwan, which are never discussed in previous publications. The frontal fold is an elongate and gentle anticlinal ridge with four-way-dip bathymetric closures in some places. Seismic data reveal prevalent and continuous bottom simulating reflectors (BSR) beneath the frontal fold, suggesting the presence of gas hydrates. Our results not only lead to assess the occurrence of gas hydrates as well as canyon incision along the frontal fold but also give insights on the interplay between gas hydrate formation and fluid migration in the frontal part of submarine accretionary wedge, in general.

Materials and methods

Seismic reflection data, high resolution bathymetry, and long piston core data are employed in this study. Seven seismic surveys were used to map the tectonic features, paleo-canyons, and BSR distribution in the frontal fold of orogenic wedge (Fig. 2). The 24-channel reflection seismic grids of MCS579 (MCS stands for Multi-Channel Seismics; the number 579 indicates the number of research cruise of R/V Ocean Researcher I), MCS716, MCS719, MCS754 and the 48-channel reflection seismic sections of MCS681 were acquired during 5 cruises onboard R/V Ocean Researcher I during 2000–2005. The 6-channel reflection seismic sections of MW9006 were collected onboard R/V Moana Wave in 1990. A long-offset, 468-channel seismic line, MGL0905-03, acquired on board R/V Marcus G. Langseth in 2009 is also used in this study.

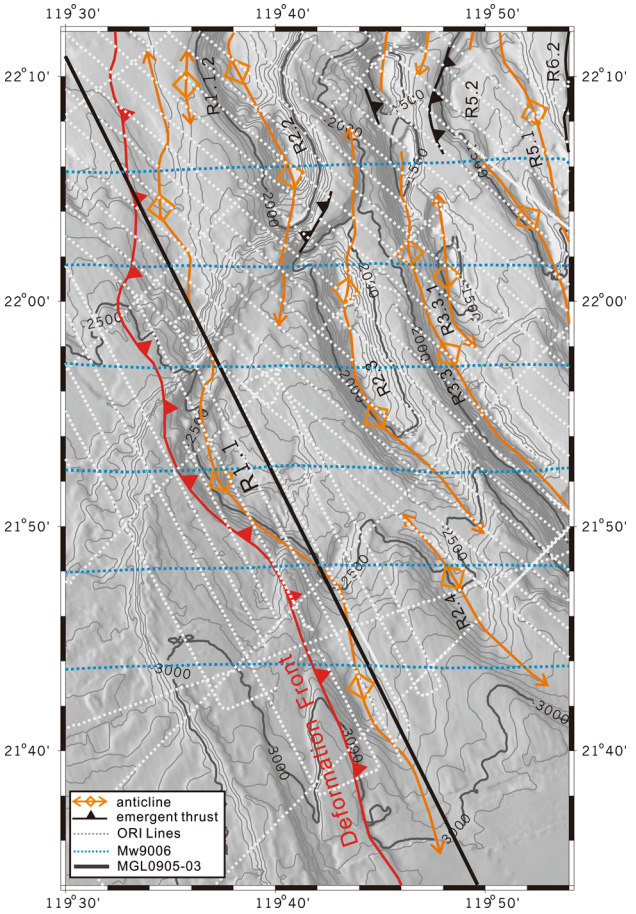

Fig. 2 Shaded relief bathymetric map and major structures of the study area. Also shown are multichannel seismic profiles used in this study. Deformation front is delineated as a barbed *red line*. Axes of anticlines are marked by *double-headed orange arrows*. The *arrows* indicate directions of plunging folds

The seismic-data recording settings of the R/V Ocean Researcher I are as follows. The channel spacing is of 12.5 m and the seismic source is a 3-airgun-array with a total volume of 475 cubic inch, which is fired at 10-s interval. The seismic signals are recorded up to 5 s. The streamer is towed at a nominal ship speed of 4.86 knots,

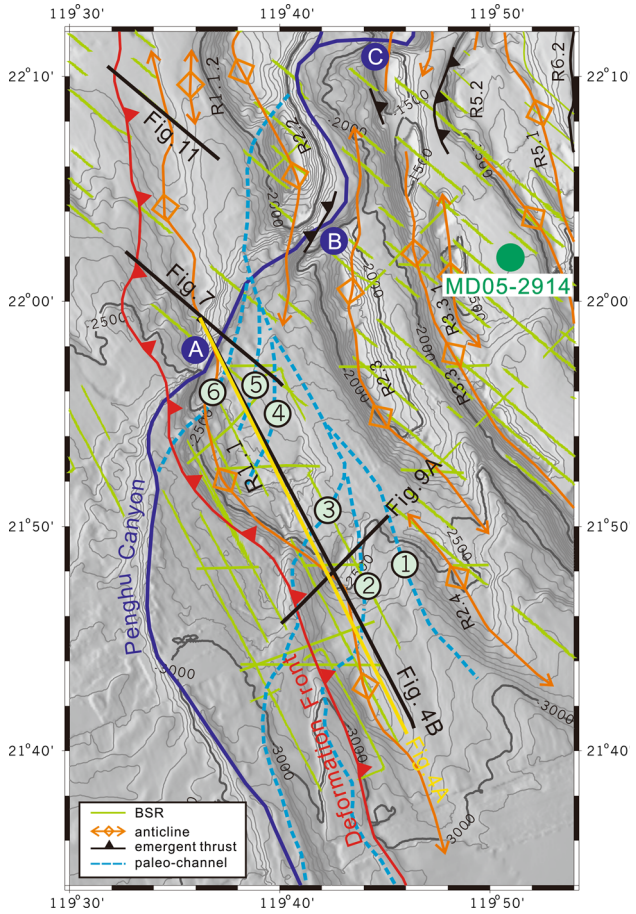

Fig. 3 Tectonic and bathymetric features along with BSR distribution in the frontal fold (R1.1) and adjacent areas. Notice that the six canyon incision are marked by *circled numbers*, 1–6. Paleo-canyons 2 and 3 exhibit relict channel morphology on the bathymetric map. *Letters A, B, C* are knickpoints of the modern Penghu canyon. The longitudinal bathymetric profile along the canyon floor is shown in Fig. 8. Three seismic profiles of MCS719-16, 716-02, and 719-09 running across the anticlinal axis of the frontal fold are shown in Figs. 7, 9, and 11, respectively. The seismic profile MCS754-18 and MGL0905-03 along strike of R1.1 structure is shown in Fig. 4. The MD05-2914 site is used to calculate the possible sedimentation rate from ^{14}C age dating

yielding a 12-fold coverage for 48-channel data and sixfold coverage for 24-channel data, respectively. The seismic recording settings for MW9006 data sets are of 25 m channel spacing and a 2-airgun-array seismic source of 420 cubic inch. The seismic signals are recorded up to 5 s and the streamer is towed at a nominal ship speed of 3.65 m/s. The seismic data recording settings of the R/V Langseth are as follows. The seismic source is a 40-airgun-array with total volume of 6,600 cubic inch. The channel spacing is 12.5 m and the maximum offset is over 6 km, yielding a 60-fold coverage for a 468-channel seismic profile.

Multi-channel seismic data of MCS579, MCS716, MCS719, MCS754 and MCS681 were processed at the Institute of Oceanography, National Taiwan University

Table 1 Results of C-14 age dating and corresponding sedimentation rate for core MD05-2914

Depth (cm)	Age (year BP)	Error (year)	Depth interval (cm)	Age interval (year)	Sed. rate (mm/year)	Events
592	1,975	71	592	1,975	3.0	Interglacial
1,267	6,464	56	675	4,489	1.5	
1,690	11,192	44	423	4,728	0.9	Deglacial
1,890	13,928	73	200	2,736	0.7	
1,990	14,468	199	100	540	1.9	Glacial
2,115	15,473	167	125	1,005	1.2	
2,690	16,765	59	575	1,292	4.5	
3,475	19,316	113	785	2,551	3.1	

The events of glacial, deglacial, and interglacial are adapted from Dansgaard et al. (1993), Lowe et al. (1994), and Turney et al. (1998), respectively. See Fig. 1 for core location

using ProMAX and SIOSEIS seismic data processing systems. Data set of MW9006 was processed at University of California, Santa Cruz and San Jose State University using the SIOSEIS processing software (Reed et al. 1992). Seismic data of MGL0905-03 was processed using Paradigm's software of Focus and Geodepth.

All seismic reflection data used in this study are processed with trace editing, spiking noise removal, water column mute, geometry, amplitude compensation, predictive de-convolution, band-pass filtering, velocity analyses for large offset MCS data (more than 700 m channel offset), normal move-out (NMO) corrections for short offset MCS data (less than 700 m channel offset), stacking, and F–K time migration with constant velocity (1,500 m/s). The velocities of NMO are based on a velocity versus sub-bottom depth function shown in Hamilton (1980).

Long piston core was recovered at site MD05-2914 during Leg 2 of MD147/MARCO POLO 1/IMAGES XII cruise of R/V Marion Dufresne in May and June, 2005. Sediments at site MD05-2914 is of ~35.14 m-long and situates at a synclinal trough of the same accretionary wedge and ~30 km to the east of the frontal fold in a water depth of 1,635 m (Figs. 1, 3). Ages for MD05-2914 sediments are dated by radiocarbon C-14 dating, and those ages are used to calculate and to infer the sedimentation rate in the study area. In order to establish the chronology of core MD05-2914, ^{14}C dating was performed on planktonic foraminifera of the cored sediments. More than 200 specimens of *Neogloboquadrina dutertrei* or *Pulleniatina obliquiloculata* (>250 μm in size) were picked from 8 levels and treated with CH_3OH and NaOCl to remove the contamination and organic matters on the foraminiferal shells. The specimens were then transformed into CO_2 gas and dated with an accelerator mass spectrometer in the

Rafter Radiocarbon Laboratory, New Zealand. All of the ^{14}C ages were calibrated using CALIB ^{14}C program (http://calib.qub.ac.uk/calib/) and presented here in calendar year BP (Table 1).

The compilation of Digital Elevation Model (DEM) offshore SW Taiwan was published in Liu et al. (1998) and is briefly described here. Compiled datasets consist mostly of swath bathymetry collected during three research cruises of (1) the 1996 ACT cruise of the R/V L'Atalante acquired using Dual EM12 system (Lallemand et al. 1997), (2) the 1995 EW9509 cruise of the R/V Maurice Ewing acquired using Hydrosweep system, (3) the 1990 MW9006 cruise of the R/V Mona Wave acquired using SeaMARC II system. The study area (i.e. the accretionary wedge offshore SW Taiwan), is almost fully covered by the ACT swath bathymetric data (see Sibuet et al. 2002 for data coverage) and therefore it attains a high spatial resolution. For other areas not covered by swath bathymetry (e.g., the northern margin of the South China Sea), underway depth sounding data (from single-beam echo sounders), and other published bathymetry datasets are used to generate the DEM (see Liu et al. 1998 for details).

Tectonic and geological setting

The area offshore SW Taiwan is in an initial stage of oblique arc-continent collision between the Luzon volcanic arc and the Eurasian plate (Huang et al. 1997; Lacombe et al. 2001). The offshore orogenic wedge in the incipient collision zone has obliquely impinged westward on the South China Sea (SCS) continental slope delineated by the deformation front and the Manila trench (Lin et al. 2008, Fig. 1). Fold-and-thrust structures of the convergent zone are predominant tectonic features of the orogenic wedge, whilst tectonic feature in the SCS slope is characterized by normal faults (Liu et al. 1997, 2004a, b). The orogenic wedge off SW Taiwan consists of upper-slope and lower-slope domains, which are separated by a significant morphologic break, probably related to the onset of multiple out-of-sequence thrusts (OOSTs) or termed splay faults in the upper-slope domain (Reed et al. 1992; Lin et al. 2009a). A series of west-vergent fold-and-thrust belts developed in the lower-slope orogenic wedge, which can be further divided into frontal and rear segments (Lin et al. 2008). The frontal segment of the lower-slope wedge is characterized by a series of elongated anticlinal ridges cored by blind thrusts, which only uplifted the strata but not break to the seafloor. By contrast, many emergent and imbricate thrusts tilted the hangingwall strata to the east as homoclinal ridges in the rear segment. The westernmost emergent thrusts and their lateral continuations are considered as the boundary separating the frontal and rear segments of the lower wedge (such as structures named R6.1, R5.1, R5.2 emergent thrusts shown in Fig. 1). In the present study, we follow the names of structures defined in Lin et al. (2008).

The study area is at the frontal fold, lying to the east of the deformation front of the accretionary wedge offshore SW Taiwan (R1.1 structure in Fig. 1). The R1.1 structure is a gentle and elongated anticlinal ridge stretching over 70 km in an NNW-SSE direction, and it diminishes its height northward toward the SCS continental slope. A main N–S-trending submarine canyon system, the Penghu canyon, also develops in the lower-slope domain. This canyon is divided into an upper-reach segment and a lower-reach segment by Yu and Chang (2002). The upper reach of Penghu canyon shows multiple tributaries joining into the main course as a fan-shaped system. Most of the upper-reach tributary canyon courses are confined by anticlinal ridges, with canyon showing V-shaped cross sections. These tributaries finally join into the main course in the lower-reach of the Penghu canyon, cutting across a series of anticlinal ridges (R1.1 and R2.2 structures, Lin et al. 2008), and turning southward and merging into the Manila trench. However, tectonic control still plays an important role for the direction of the course and shifting of the Penghu canyon (Yu and Hong 2006).

Results

Seismic and topographic features of modern Penghu canyon and paleo-canyons

The R1.1 structure is an anticlinal ridge uplifted by the youngest thrusting of orogenic wedge. Modern Penghu submarine canyon cuts across the middle part of R1.1 structure in an NE-SW direction and then turns to the south direction. Bathymetric data also shows a few abandoned paleo-channels which can be identified by peaks of v-shaped bathymetric contours pointing to an upslope direction near or above the R1.1 structure. These abandoned canyons showing relict linear depressions, correlatable to seismic sections, can be found along paleo-canyons marked as numbers 1, 2, 3, 6 shown in Fig. 3; paleo-canyons numbered as 4 and 5, respectively, are buried features without bathymetric expressions. Seismic facies of cut-and-fills are present beneath the paleo-canyon courses and along the frontal fold as evidenced by many seismic sections. For example, seismic profile of MCS754-18, locating along-strike the R1.1 structure, shows a series of paleo-canyon infills developed on upper part of the anticline (middle and lower figures of Fig. 4). Similar characteristics of channel cut-and-fills also can be clearly seen on the seismic profile of MGL0905-03, which is very close and

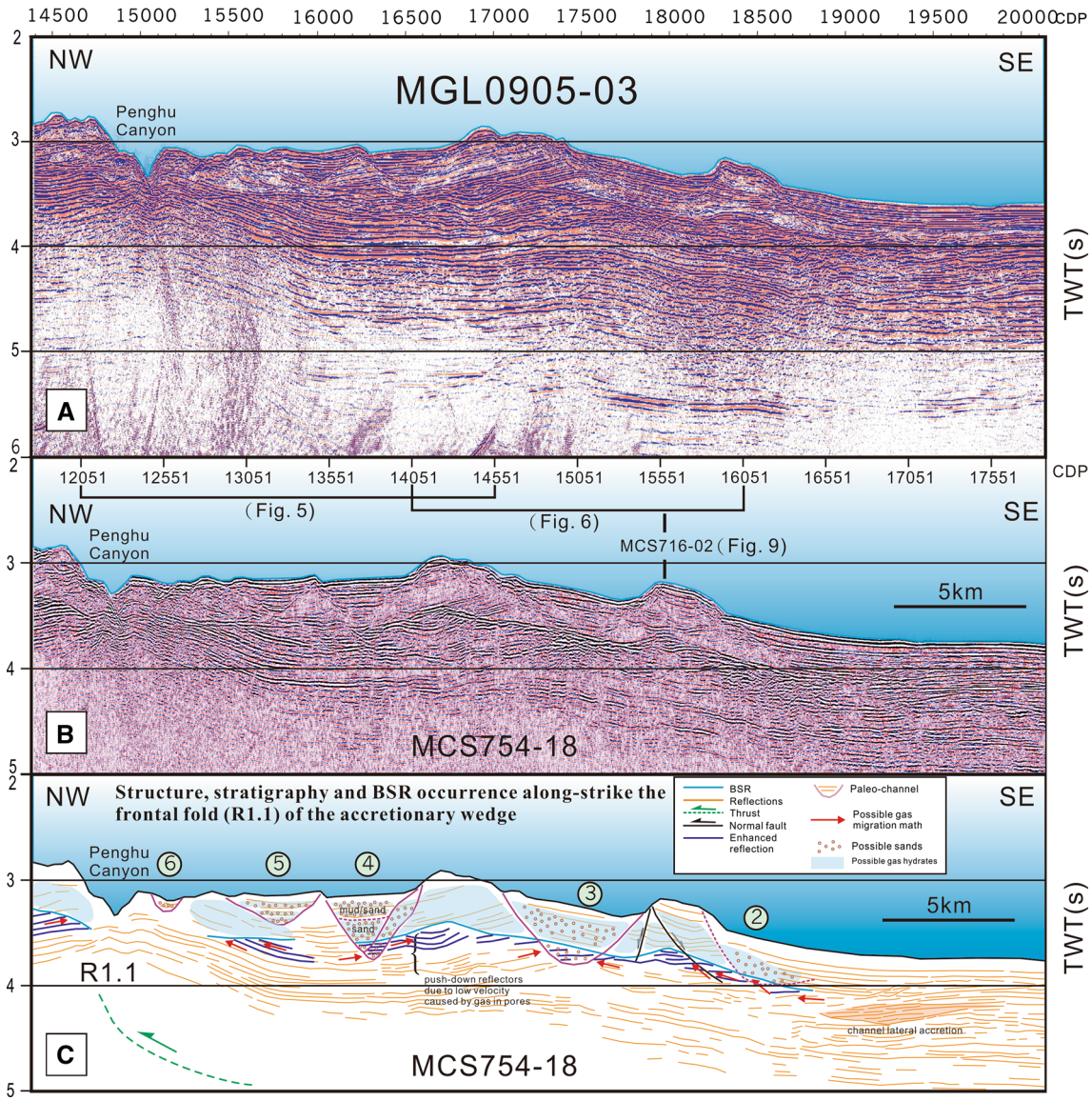

Fig. 4 Uninterpreted seismic profiles MGL0905-03 (**a**), MCS754-18 (**b**), and interpreted profile (**c**) of MCS754-18. The two seismic lines run along-strike the axis of frontal fold (R1.1) as shown in Fig. 3. A series of paleo-canyon infills is found along the upper part of anticline (enlarged sections showing canyon infills are shown in Figs. 5, 6). Note that continuous BSRs exist below the channel infills. The lower parts of channel infills are inferred to be sand-rich sediments, favorable to host an appreciable amount of gas hydrates. The push-down reflectors are interpreted to result from gas-charged sands below BSRs. The seismic profile MCS716-02, running perpendicular to the R1.1 anticline is shown in Fig. 9

perpendicular to seismic line MCS754-18 (upper figure of Fig. 4). Figures 5 and 6 are enlarged sections of canyon infills for paleo-canyon 3 to paleo-canyon 6.

Paleo-canyon 3 (Figs. 4, 6) is characterized by a broad and U-shaped canyon profile with outward-dipping reflectors interpreted as levee deposits on both sides of the canyon, indicating an aggradational channel. An aggradational channel is developed by turbidity currents of low energy due to reduction in flow size, density, or an increase in sediment grain-size (e.g., Kneller 2003). Turbidity currents in an aggradational channel system deposit sediments both in the channel axis and overbank areas in the levees (Kneller 2003). The channel infills for paleo-canyon 3 are interpreted to be sand-prone especially in the lower part. From Fig. 6, one finds that a cluster of strong reflections exists exclusively beneath the BSR and above the canyon incision marked by a blue dashed line. This feature indicates that paleo-canyon 3 incises into mud-prone sediments showing no strong stratal reflections beneath BSR; while the canyon itself is filled by permeable sediments in the lower part as evidenced by gas charged sediment pocket (and hence strong reflections) beneath the BSR. Figure 6

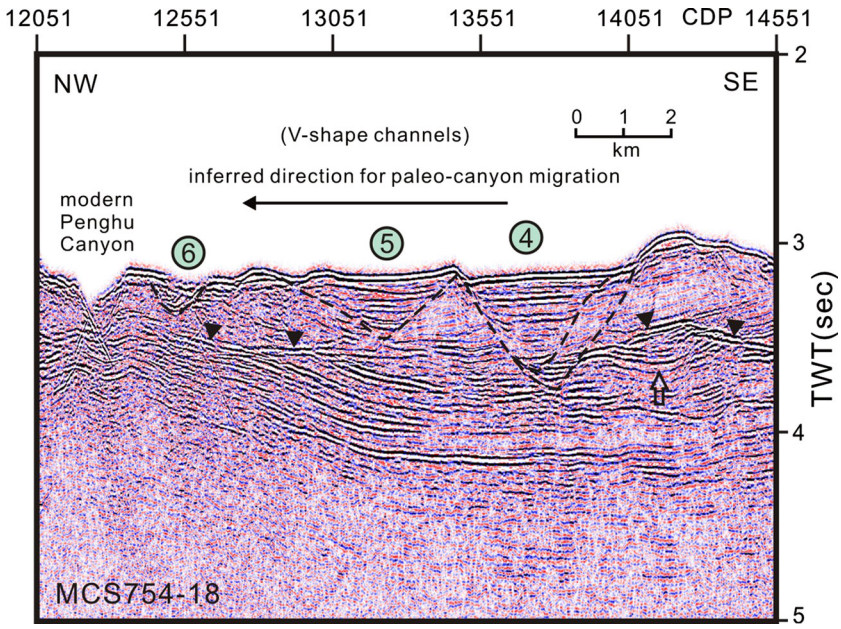

Fig. 5 Seismic profile, MCS754-18, showing paleo-Penghu canyon (canyons 4, 5, 6). The canyon incisions are marked by *black dashed lines*. See Fig. 4 for profile location. Locations of BSR are marked by inverted triangles. The pocket of push-down reflectors beneath a bathymetric ridge is marked by an *open arrow*

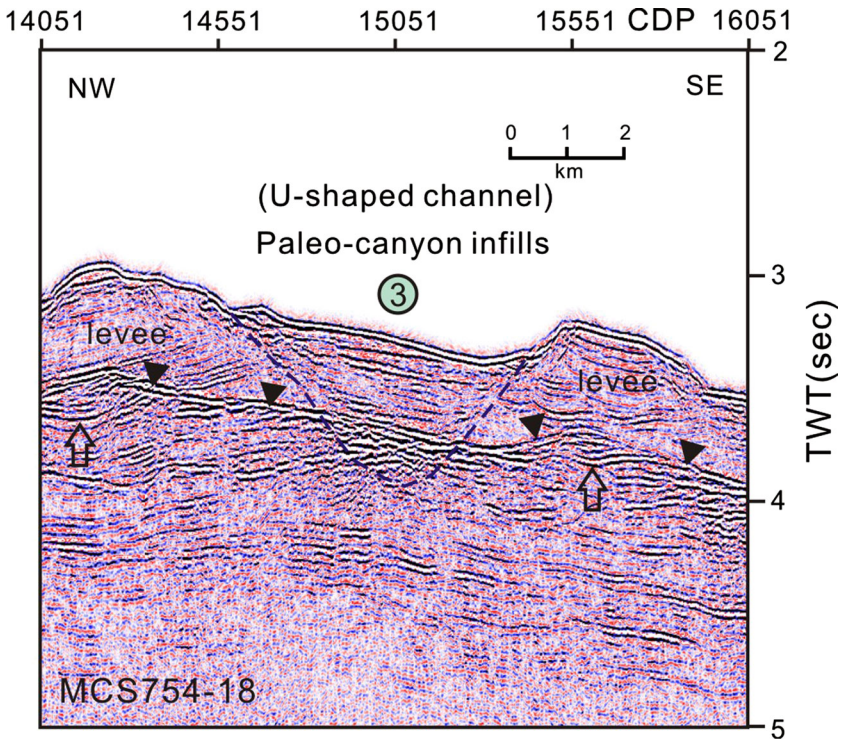

Fig. 6 Seismic profile, MCS754-18, showing the earlier stage of paleo-Penghu canyon. See Fig. 4 for profile location. Locations of BSR are marked by *inverted triangles*. The pockets of push-down reflectors beneath bathymetric ridges are marked by *open arrows*. Base of canyon is marked by a *dashed line*. Note that the bright reflections within paleo-canyon 3 and beneath the BSR may indicate gas-charged coarse sediments existing at the lower part of the canyon infills

also shows that there is a series of strong reflections existing in the northern levee of paleo-canyon 3. A BSR cuts across these north-dipping strong reflections. Above the BSR, the strong reflections are parallel in character and becoming push-down reflectors beneath the BSR. This feature is likely to indicate that strong reflections are highly permeable beds with gas-charged layers (and hence push-down reflectors) beneath the BSR, suggesting that the levee deposits of paleo-canyon 3 contain some permeable beds. Note that we have carefully checked the polarity of waveforms for both seafloor and BSR using both Petrel and Kingdom seismic interpretation software and found that the polarity is reversed to each other.

Paleo-canyons 4, 5, 6 (lying to the north of paleo-canyon 3) are V-shaped canyon-incisions without levees (Fig. 5). Paleo-canyon 4 (Fig. 5) shows that a second canyon re-incised the original canyon infills, indicating a lateral-migration of the thalwegs from SE to NW. There is also a

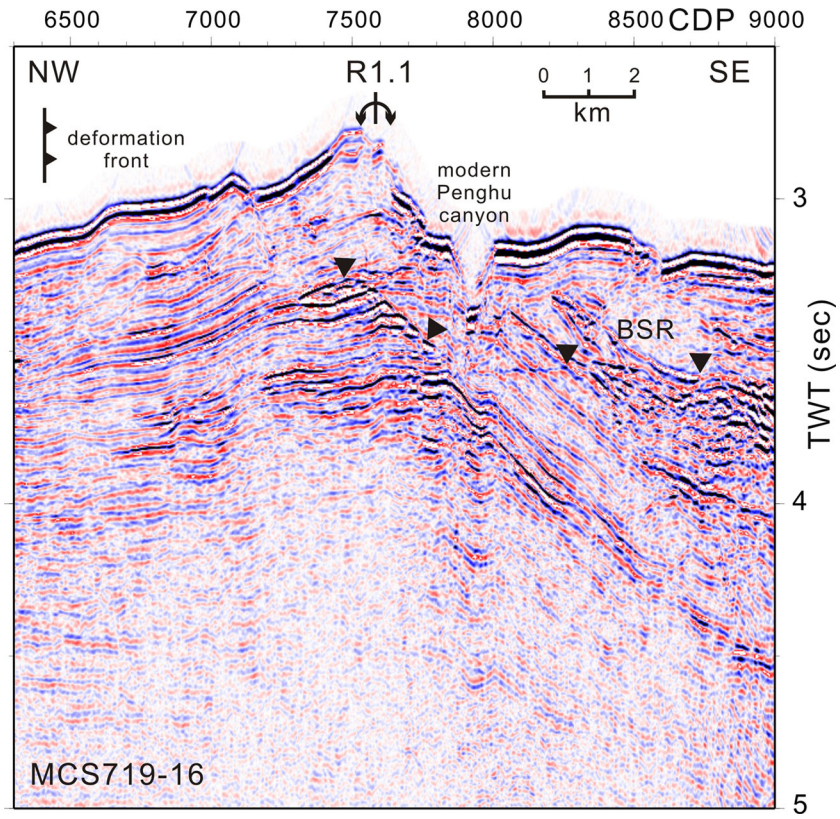

Fig. 7 Seismic profile, MCS719-16, showing that the frontal fold has been cut by the modern Penghu submarine canyon. The *V-shaped* canyon profile indicates that the rate of fold uplift is greater than that of canyon incision. See Fig. 3 for profile location

tendency that the width and depth of canyon incision decrease from south to north along the hinge line of frontal fold. Figure 4 shows this feature for paleo-canyon 3 to paleo-canyon 6. These V-shaped canyons (i.e., paleo-canyons 4, 5, 6, Fig. 5) are characteristic erosional canyons, resulting from base level falls, caused, most likely, by uplift of the frontal fold and accretionary wedge. Base level in a turbidite system is determined by gravity base, the lowest point that turbidity currents can flow to (Pirmez et al. 2000; Kneller 2003). Falling of base level leads to an increased gradient of canyon and therefore an increased rate of down-cutting by turbidity currents (Flood and Piper 1997). Erosional canyons may be also resulted from higher density and greater thickness of turbidity currents (Kneller 2003). These erosional canyons will not form levees because of no aggradation occurred. However, erosive canyons often host thin tractional lag deposits at the bottom part of canyon infills. The tractional deposits are mostly coarse sediments, like the lower part of canyon infills of paleo-canyon 4 shown in Fig. 5. The upper and most part of erosive canyon-infills are often characterized by hemipelagic sediments.

The modern courses of Penghu submarine canyon are mostly confined in bathymetric lows between tectonic ridges. The lower reach of the canyon generally cuts across tectonic ridges, however, such as structures/ridges of R1.1, R2.2, and R3.3 as shown in Fig. 3. Seismic profile MCS719-16 shows that the frontal fold has been cut by modern Penghu submarine canyon, showing a narrow and V-shaped canyon profile (Fig. 7). The longitudinal bathymetric profile along the modern Penghu submarine canyon course also shows three knickpoints (A, B, C) of bathymetric relieves as shown in Figs. 3 and 8. The three knickpoints correspond to the positions of three inferred active folds (i.e., structures R1.1, R2.2 (backthrust), and R3.3). These bathymetric anomalies along Penghu canyon course indicate that the rate of fold uplift is greater than rates of erosion along the canyon path, which is similar to knickpoints observed along canyons in the Barbados accretionary wedge (e.g., Huyghe et al. 2004) and in other prisms (e.g., Pirmez et al. 2000; Mitchell 2006; Mouchot et al. 2010). The observation that the amount of offset at knickpoint A is greater than that at knickpoints B and C suggests the rate of uplift at fontal fold is greater than that at structures R2.2 and R3.3 (Fig. 8). The significant bathymetric break ($\sim$300 m) at knickpoint A suggests a very active tectonic uplift of the frontal fold.

BSR occurrences and underlying free-gas indicators

A bottom simulating reflector (BSR) is a phase-reversed reflection event, indicating the base of gas hydrate stability zone (Shipley et al. 1979; Yuan et al. 1996) as evidenced by many scientific boreholes (e.g., boreholes in the

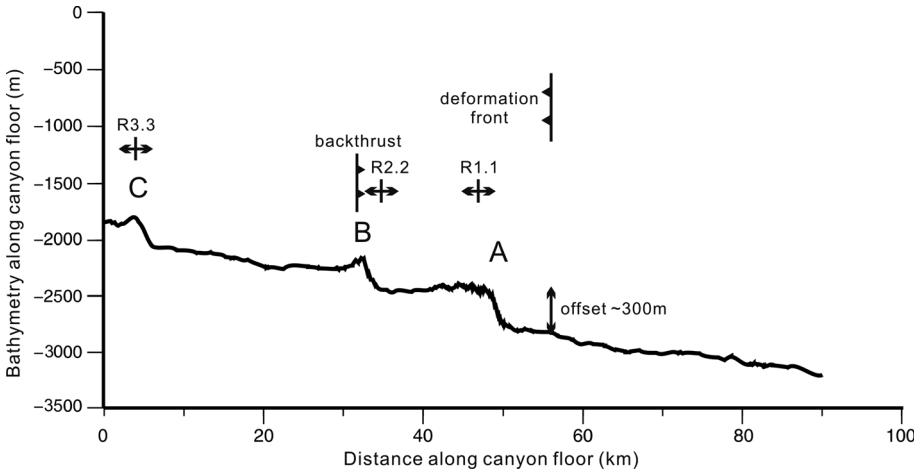

Fig. 8 The longitudinal bathymetric profile along the Penghu submarine canyon in the study area (see Fig. 3 for profile location). *Letters A, B, C* indicate three knickpoints along the canyon, corresponding to the positions of three active folds (i.e., structures R1.1, backthrust of R2.2, and R3.3). The significant bathymetric break (~300 m) at the knickpoint A suggests a very active tectonic uplift for the frontal fold

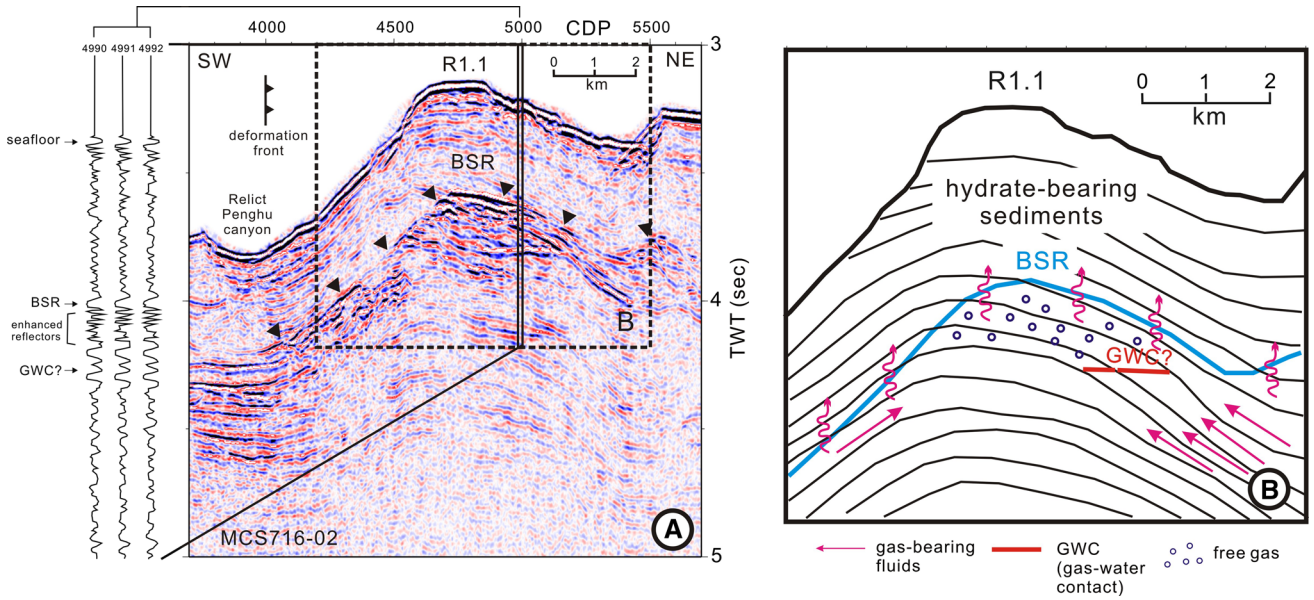

Fig. 9 Uninterpreted seismic profile (**a**) and interpreted profile (**b**) of MCS716-02 showing the continuous BSR (*blue line*) and underlying flat spot. The flat spot is a horizontal and enhanced reflector, cutting across a few dipping reflectors, interpreted as a gas–water contact (GWC). Three seismic wavelets at CDPs 4990–4992 are displayed on the left of the uninterpreted seismic profile. Notice that the phase of BSR waveform is reversed to that of the seafloor and GWC. Straight and wiggled *arrows* indicate possible gas-charged fluid migration pathways by advection and diffusion processes, respectively. Profile location is shown in Fig. 3

northern Gulf of Mexico, Boswell et al. 2012). The BSR referred here is defined as strong reflections running approximately parallel to the seafloor and cross-cutting stratigraphy though BSRs may be defined differently in other study areas (see Mosher (2011), for example). The widespread occurrence of BSRs beneath the frontal fold suggests the likely existence of gas hydrates (Fig. 3). Seismic data also reveal several lines of evidence for the prevalent existence of free gas beneath BSRs. For examples, a few enhanced reflectors exist below BSRs interpreted as free gas-charged sediments beneath the gas hydrate stability zone (Fig. 4). Some of the enhanced reflectors show "push-down" characteristics due, most likely, to lowered velocity caused by a higher concentration of free gas in sediments, for examples, beneath CDPs around 14,050 and 15,550 of MCS754-18 shown in Fig. 4. Seismic profile MCS716-02, running perpendicular to the frontal fold, shows continuous BSR and "flat spot" below BSR (Fig. 9a). The flat spot is a horizontal and strong reflector lying beneath the east limb of the anticline and cross-cutting a few east-dipping reflectors. A flat spot is conventionally interpreted as a gas–water contact (Brown 2004; Løseth et al. 2009). Three example seismic wavelets in Fig. 9a show that the phase of BSR waveform is reversed to that of the seafloor and the flat spot. The phase of wavelets of seafloor and the flat spot are the same

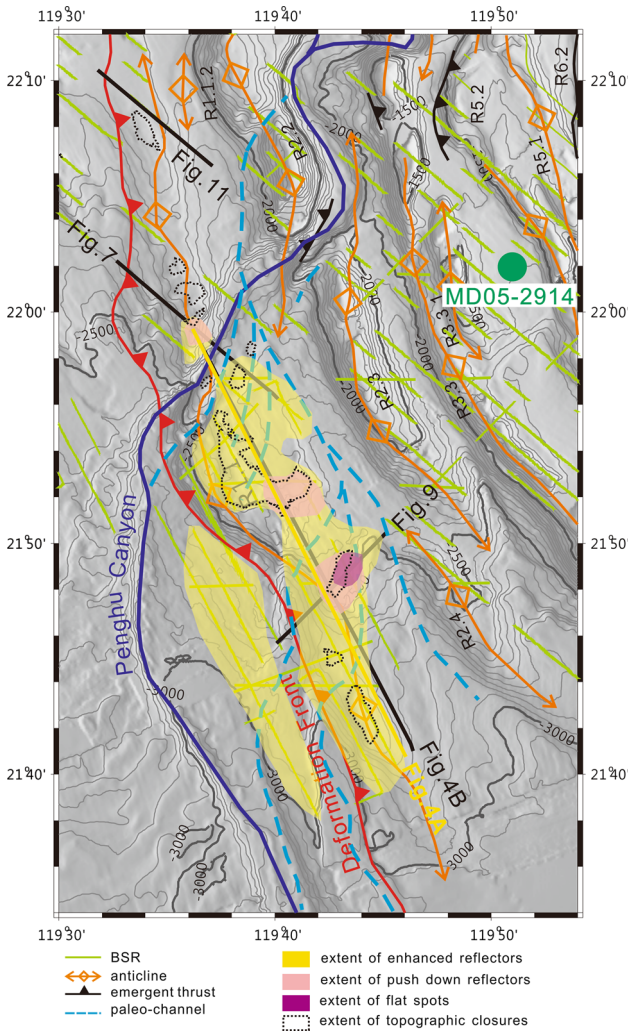

Fig. 10 Distribution of BSRs and underlying enhanced reflectors, push-down reflectors, and flat spots in the study area. Notice that distribution of BSRs, enhanced reflectors, and push down reflectors correspond especially to the topographic closure in the southern part of R1.1 structure

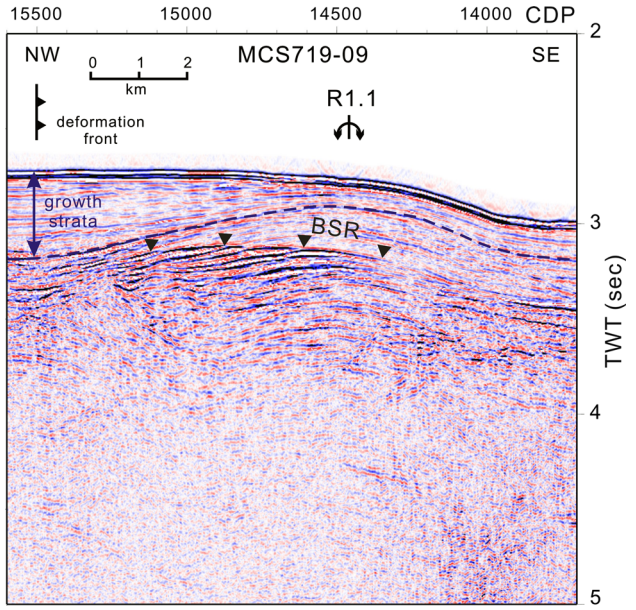

Fig. 11 Seismic profile, MCS719-09, showing the northernmost of R1.1 anticlinal structure. The growth strata marked on the *left* between R1.1 and continental slope is used to estimate the initial age of uplift for this frontal fold. The *blue dashed line* marks the base of growth strata that onlap the deformed strata. BSRs are marked by *inverted triangles*

because their seismic waves propagate from lower-velocity medium above (water for the seafloor and gas-charged sands for the flat spot) to higher-velocity medium below (water-bearing sediments both beneath the seafloor and the flat spot). By contrast, the wave propagation across BSR is from high- to low-velocity mediums (i.e., hydrated sediments above to gas-charged sediments below). The presence of the flat spot suggests the existence of natural gas in reservoirs. We therefore interpret that the flat spot is a gas–water contact (GWC, Fig. 9b).

All the above seismic anomalies related to the presence of gas hydrates or free gas in the frontal fold (i.e., BSR, enhanced reflections beneath BSR, push-down reflectors beneath BSR, flat spot beneath BSR) are mapped out as shown in Fig. 10. Most of the distributions of BSRs, enhanced reflectors, push-down reflectors, and flat spot correspond to the extent of topographic closures (i.e. relative higher areas lying above the deepest and closed bathymetric isobath) or the locations of paleo-canyons along the hinge of frontal fold, especially on the southern part of the frontal fold. We therefore conclude that favorable conditions for forming thick gas hydrates and underlying free gas exist beneath the frontal fold.

Timing for the initial uplift of frontal fold

The initial thrusting age for the frontal fold can be estimated by the thickness and sedimentation rate of the growth strata between the frontal fold and the South China continental slope (Fig. 11). Seismic profile, MCS719-09, shows the northernmost structure of the R1.1 anticline. The growth strata can be identified as a divergent sediment wedge delimited by an onlapping surface at its base on the west flank of the fold. Beneath this onlapping surface, seismic reflectors are parallel in character with constant thickness beneath the frontal fold and its adjacent trough areas, indicating those sediments were deposited before folding of R1.1 structure. The growth strata were formed by continuous deposition during the growth of frontal fold. Similar growth strata related to folding or thrusting are commonly found in modern accretionary wedge (e.g., Grando and McClay 2007) or in deformed foreland successions (e.g. Burbank and Verges 1994). The maximum thickness of the growth strata is believed to record the

complete and continuous sequence of strata since the initial thrusting of frontal fold. There is, however, a little uncertainty for the exact position for the basal growth strata at the synclinal trough as it coincides with BSR and enhanced reflections on the profile (Fig. 11).

The age for the basal growth strata indicate the age of initial thrusting of the frontal fold. This age can be approximated by the maximum thickness of the growth strata divided by the sedimentation rate in this area. For obtaining sediment thickness from seismic sections, one needs to convert seismic travel times into depths using a reasonable sediment velocity function. The sedimentation rate and the sediment velocity function are therefore two important parameters for performing this calculation. Ideally these two parameters would be obtained directly from the growth strata. Because there is no deep borehole penetrating into this growth strata, we use the sedimentation rate obtained from a nearby giant piston core, MD05-2914, locating at an adjacent slope basin (Fig. 1), and a sediment velocity function obtained from the FJ-1 well, drilled in the adjacent shelf. We note that our calculation for the initial thrusting age for the frontal fold may not be an exact solution but an approximation because these two parameters are derived from nearby areas and not directly from the growth strata.

The sediment velocity profile from FJ-1 well is located at a water depth of 87 m and drilled by CPC Corporation, Taiwan (Figs. 1, 12). Sediments of FJ-1 well are dominated by Plio-Pleistocene mudstone (Lin et al. 2003), and similar lithology is expected to be found in the growth strata west of the frontal fold as both locations lie in the same shelf and slope setting. One may argue that the deep water growth strata related to frontal fold and shelf sediments drilled in the FJ-1 well may show very different sediment velocity profiles as they were accumulated in very different water depths (around 2,000 m water depth for growth strata versus less than 200 m water depth for shelf sediments drilled at FJ-1 well). In order to clarify the arguments that sediment velocity functions may vary with water depths, we chose a sediment velocity profile from ODP Site 1,148 (Cheng et al. 2004), which is drilled at a water depth of 3,294 m, for comparison. The dominant lithology at Site 1148A is Oligocene-Recent mudstone (Li et al. 2004) and is similar to FJ-1. Therefore we are comparing sediment velocity profiles for similar lithology but lies at shelf and deep water settings. Figure 12 shows two superimposed sediment velocity profiles lined up at the seafloor depth. The sonic velocities from both boreholes correspond well to each other regardless the large difference in water depth. Only the sonic velocity in 400–500 m depth of Site 1148A

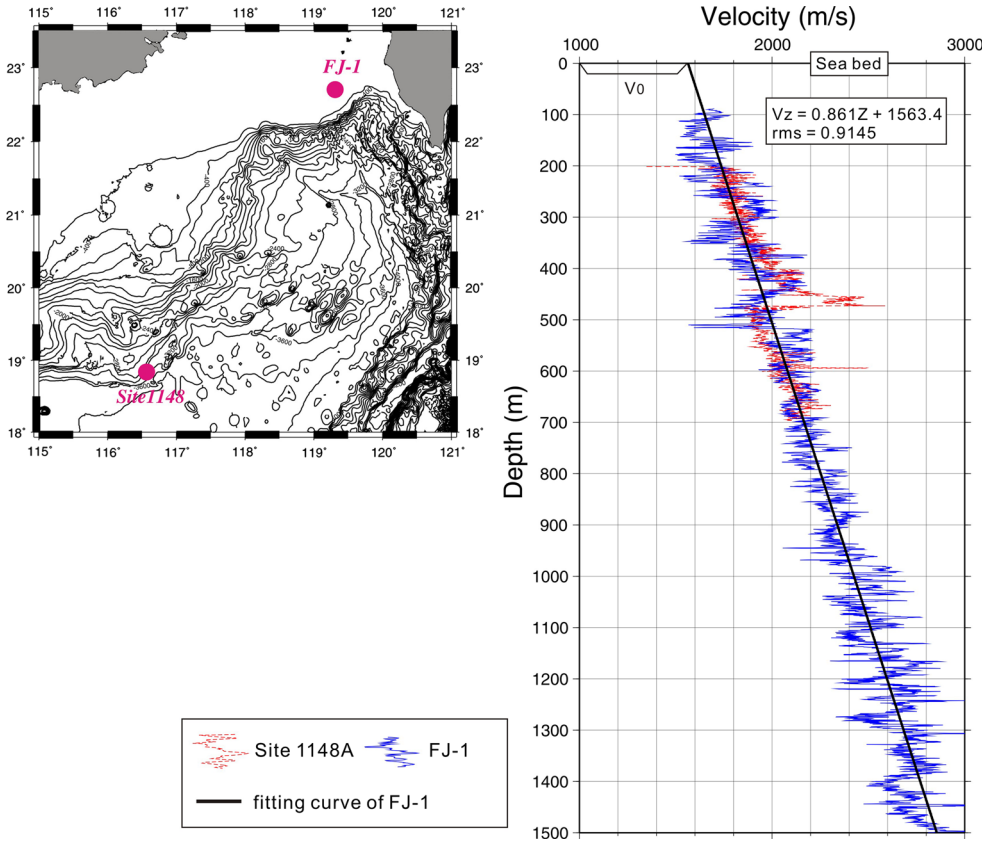

Fig. 12 Comparison of sonic velocities in the sediments in different water depths of ODP site 1148A (water depth ~3,294 m, Cheng et al. 2004) and FJ-1 (water depth ~87 m, Lin et al. 2003). The fitted trend of FJ-1 (the *black line*) corresponds well to the sonic velocity of both wells. The formula of the *trend line* is shown on the upper right corner of the figure. Locations of ODP site 1,148 and FJ-1 well are shown in the inset figure. *rms* root mean square

is anomalously large owing to the existence of gas hydrates as suggested by Wu et al. (2007). Similar velocity functions at both shallow and deep water depths indicate that the increase of sediment velocity with increasing depths is due mainly to sediment compaction for mudstone. We conclude, from this comparison, that sediment compaction curves at both wells are similar because of similar lithology even though a large difference in water depths; and the sediment velocity function for the deep-water growth strata related to the studied frontal fold can be approximated by FJ-1 well from the adjacent shelf. The velocity trend (black line in Fig. 12) that best describes the sonic log profile of FJ-1 can be expressed as:

$$V_z = 0.861Z + 1563.4$$

where Z is the sub-bottom depth of sediment, V_z, the sonic velocity at depth Z. Comparing above formula to that of Reilly (1993):

$$V_z = V_0 + KZ$$

where V_0 is the sonic velocity of sediments at seabed, K is the rate of increasing sediment velocity with increasing sub-bottom depth, and therefore V_0 corresponds to 1,563.4 m/s and K to 0.861. These two parameters and the thickness of growth strata obtained from seismic profile in seismic one-way-travel time (t) can be substituted into the time-depth conversion formula of Smallwood (2002):

$$Z_{bt} = \frac{V_0}{K}\left(e^{Kt} - 1\right)$$

where Z_{bt} (in m) is the thickness of growth strata. Finally, the thickest growth strata can be calculated to be around 430 m in thickness.

For the parameter of sedimentation rate, a giant piston core of MD05-2914 (~35.14 m long) located at a synclinal trough lying in between anticlinal ridges of R3.3.1 and R5.2 structures is used to derive the sedimentation rate for calculating the initial thrusting age of the frontal fold. The sediments are dated from ^{14}C datings on forams as detailed in Sect. 2. Table 1 shows the dating results from MD05-2914. The sedimentation rate for each stratigraphic level can be calculated from depth interval divided by corresponding age interval (Table 1). The result shows that the sedimentation rates vary in a range of 0.7–4.5 mm/year.

We notice that low sedimentation rates occur in depths between 1,267–1,690 cm and 1,690–1,890 cm. Ages of these depth intervals range from around 6,464–13,928 year BP, corresponding to the most recent rise of global sea-level (e.g., Liu et al. 2004a, b; Martinson et al. 1987; Chappell et al. 1996). The last eustatic rise occurred during the most recent deglacial from the last glacial maximum (LGM) to the Holocene (Jansen et al. 2007). Higher sedimentation rates are found during glacial (~19,316–14,468 year BP) and interglacial (since ~6,464 year BP) periods. The maximum and minimum depositional ages for the 430-m thick growth strata can be calculated by using the lowest and the highest sedimentation rates (i.e., 0.7 and 4.5 mm/year, respectively, Table 1) and this practice yields a maximum and minimum ages of 614 and 96 kyr, respectively. The result suggests that the 430-m thick growth strata must have been accumulated during several cycles of eustatic sea-level changes and using one particular sedimentation rate obtained from one segment of a full sea-level cycle will not be an inappropriate approach. We therefore apply an averaged sedimentation rate obtained from MD05-2914 (i.e., 1.8 mm/year) for calculating the oldest age, a proxy for age of initial thrusting, for the growth strata. With known sediment thickness (i.e., 430 m thick) and inferred average sedimentation rate (i.e. 1.8 mm/year), the initial age of uplifting for the frontal fold is calculated to be around 0.24 Ma.

Discussion

There is a clear link between the presence of BSRs and the frontal fold. BSRs are prevalent beneath the highline of the frontal fold and cluster especially beneath topographic highs. In addition, flat spots, enhanced reflectors and push-down reflectors beneath BSRs, exist especially beneath topographic four-way dip closure. This indicates that topographic closures exert a second-order control on gas hydrate distribution. This patchy occurrence of gas hydrates and free gas-related features may also indicate nearby efficient conduits, and therefore gas escape, among others. Stratigraphic controls on gas hydrate occurrences are also evident on canyon-incisions. The multiple paleo-canyon infills developed along the southern part of this fold may provide thick and porous sands to host a large amount of gas hydrates and underlying free gas beneath the fold. Several wide topographic closures in the southern part of the fold may also help to trap abundant free gas beneath the four-way-dip closures.

As methane gas dissolves in sediment pore water, the gas-bearing fluids may migrate upward along dipping permeable sediments (e.g., sand layers) to the gas hydrate stability zone and form gas hydrates (Hyndman and Davis 1992). Brittle fault zones are also good migration conduits for deep-seated, gas-bearing fluids (Caine et al. 1996). Previous studies (e.g., Moore et al. 2001) indicate that the decollement surface in the accretionary wedges is the major fluid migration conduits. The frontal fold situates at the top and end of an east-dipping decollement surface, a major migration pathway for gas-bearing fluids; and this fold is also the most distal and final structural traps for

upward migrating gas. It is reasonable to infer that the above two factors make the frontal fold as the final site of upward-migrating gas. In addition, a series of canyon cut-and-fills presumably sand-prone in the lower part existed along the frontal fold, together with the fold/structural trap has been formed since ~0.24 Ma, a relatively old thrust-initiation age comparing to its onshore counterpart of the Tiechanshan (TCS) gas field (see below), these two factors may further lead to the prevalent existence of gas hydrates and free gas beneath the frontal fold.

An analytical fold model suggests the initial thrusting age for the Pakuashan anticline (PKS in the index figure of Fig. 1), the frontal fold in onshore central Taiwan, to be around 0.06 Ma (Simoes et al. 2007), which is much younger than that of the frontal fold in the study area (i.e. 0.24 Ma). Forty kilometers northward along the PKS anticline, there exists the Tiechanshan anticline (TCS in the index figure of Fig. 1) that marks the same frontal fold. The TCS is the largest gas field in Taiwan with around 1 Trillion Cubic Feet (TCF) of recoverable thermogenic gas (Yang et al. 1994). Given the close proximity of the PKS and the TCS anticlines, the age of initial folding for the TCS gas field is regarded as comparable to that of the PKS anticline (i.e. 0.06 Ma). Note that the relatively short duration for the existence of the TCS structural trap, it still traps an appreciable amount of natural gases. The frontal fold (or R1.1 structure) in the study area is formed since 0.24 Ma, which is much older than the TCS anticline. We speculate that, given the longer time span than its onshore counterpart, the frontal fold off SW Taiwan may host even larger amount of hydrocarbons than the TCS gas field if favorable conditions exist. The exact amount of gas-in-place beneath the R1.1 structure warrants a detail assessment and this is beyond the scope of this study. However, an array of geophysical evidences (e.g., BSRs, enhanced reflections, push-down reflections, flat spots) tend to suggest gas hydrates and free gas are likely to exist widely beneath the frontal fold.

Conclusions

We recognize anticlinal features, paleo-canyons and several indicators for the existence of gas hydrates and their associated underlying free gas in the frontal fold of accretionary wedge off SW Taiwan. There are six distinct canyon/channel infills around the frontal fold. The uplift of the frontal fold results in a significant knickpoint of ~300 m relief on the bathymetry along the thalweg of the modern Penghu canyon. The initial uplift age for the frontal fold is around 0.24 Ma, estimated using the thickness of the growth strata in the west flank of the frontal fold and sedimentation rate determined from MD05-2914 core samples in a nearby area.

A widespread occurrence of BSRs has been recognized from seismic images beneath the frontal fold, suggesting a prevalent existence of gas hydrates in the study area. A few gas indicators such as enhanced reflectors, push-down reflectors, and flat-spots shown on seismic sections also indicate a substantial quantity of free gas is likely to present beneath the gas hydrate stability zone. We suggest that the multiple paleo-canyon infills beneath the frontal fold may provide porous sands to host a large amount of gas hydrates above BSRs and free gas below BSRs. Several areas of topographic closures in the southern part of the frontal fold may help to trap free gas beneath the structure. Our results indicate that the toe of accretionary wedge offshore SW Taiwan is a dynamic hydrogeologic environment, which is likely to trap substantial amounts of hydrocarbons under favorable conditions.

Acknowledgments We would like to thank the crews of the R/V Ocean Researcher I, R/V Moana Wave, and R/V Langseth in collecting the seismic data used in this study. We thank L.S. Teng, S.-K. Hsu, and W.-C. Chi for their suggestions and opinions for improving the quality of this paper. Julien Bourget read an earlier draft of this paper and made substantial comments to improve the quality of this paper. We thank reviewers J.-C. Sibuet and T. Byrne for their constructive comments. This study is supported by Central Geological Survey, Ministry of Economic Affairs, Taiwan and a project sponsored by National Science Council under the grant of NSC 102-3113-P-002-036.

References

Boswell R, Collett TS, Frye M, Shedd W, McConnell DR, Shelander D (2012) Subsurface gas hydrates in the northern Gulf of Mexico. Mar Petrol Geol 34:4–30

Brown AR (2004) Interpretation of three-dimensional seismic data (six edition). AAPG Memoir 42 SEG investigations in geophysics No 9:534 pp

Burbank DW, Verges J (1994) Reconstruction of topography and related depositional systems during active thrusting. J Geophys Res 99(10):20281–20297

Caine JS, Evans JP, Forster CB (1996) Fault zone architecture and permeability structure. Geology 24:1025–1028

Cawood PA, Kroner A., Collins WJ, Kusky TM, Mooney WD, Windley BF (2009) Accretionary orogens through Earth history. In: Cawood PA, Kroner A (eds) Earth accretionary systems in space and time. Geol Soc, London, Spec Publ 318, pp 1–36

Chappell J, Omura A, Esat T, McCulloch M, Pandolfi J, Ota Y, Pillans B (1996) Reconciliation of late Quaternary sea levels derived from coral terraces at Huon Peninsula with deep sea oxygen isotope records. Earth Planet Sci Lett 141:227–236

Cheng X, Zhao Q, Wang J, Jian Z, Xia P, Huang B, Fang D, Xu J, Zhou Z, Wang P (2004) Data report: Stable isotopes from Sites 1147 and 1148. In: Prell WL, Wang P, Blum P, Rea DK, Clemens SC (eds) Proceedings of ODP, Sci. Results 184: College Station, TX (Ocean Drilling Program), 1–12

Chi WC, Reed DL, Tsai CC (2006) Gas hydrate stability zone in offshore southern Taiwan. Terr Atmos Ocean Sci 17:829–843

Chuang CY, Yu HS (2002) Morphology and canyon forming processes of upper reach of the Penghu submarine canyon off southwestern Taiwan. Terr Atmos Ocean Sci 13:91–108

Cooper M (2007) Structural style and hydrocarbon prospectivity in fold and thrust belts: A global review. In: Ries AC, Butler RWH, Graham RH (eds) Deformation of the continental crust: the legacy of Mike Coward. Geol Soc, London, Spec Publ 272, pp 447–472

Dansgaard W, Johnsen SJ, Clausen HB, Dahl-Jensen D, Gundestrup NS, Hammer CU, Hvidberg CS, Steffensen JP, Sveinbjörnsdottir AE, Jouzel J, Bond G (1993) Evidence for general instability of past climate from a 250-kyr ice-core record. Nature 364:218–220

Flood RD, Piper DJW (1997) Amazon fan sedimentation: the relationship to equatorial climate change, continental denudation, and sea-level fluctuations. In: Flood RD, Piper DJW, Klaus A, Peterson LC (eds) Proceedings of ODP, Sci. Results 155: pp 653–675

Grando G, McClay K (2007) Morphotectonics domains and structural styles in the Makran accretionary prism, offshore Iran. Sed Geol 196:157–179

Hamilton EL (1980) Geoacoustic modeling of the sea-floor. J Acoust Soc Am 68:1313–1340

Huang CY, Wu WY, Chang CP, Tsao S, Yuan PB, Lin CW, Xia KY (1997) Tectonic evolution of accretionary prism in the arc-continent collision terrane of Taiwan. Tectonophysics 281:31–51

Huyghe P, Foata M, Deville E, Mascle G, Caramba Working Group (2004) Channel profiles through the active thrust front of the southern Barbados prism. Geology 32(5):429–432

Hyndman RD, Davis EE (1992) A mechanism for the formation of methane hydrate and seafloor bottom-simulating-reflectors by vertical fluid expulsion. J Geophys Res 97:910–924

Jansen E, Overpeck J, Briffa KR, Duplessy JC, Joos F, Masson-Delmotte V, Olago D, Otto-Bliesner B, Peltier WR, Rahmstorf S, Ramesh R, Raynaud D, Rind D, Solomina O, Villalba R, Zhang D (2007) Palaeoclimate. In: Solomon S, Qin D, Manning M, Chen Z, Marquis M, Averyt KB, Tignor M, Miller HL (eds) Climate change 2007: the physical science basis. Contribution of working group I to the fourth assessment report of the intergovernmental panel on climate change. Cambridge University Press, Cambridge, United Kingdom and New York, NY

Kneller B (2003) The influence of flow parameters on turbidite slope channel architecture. Mar Petrol Geol 20:901–910

Lacombe O, Mouthereau F, Angelier J, Deffontaines B (2001) Structure, geodetic, and seismology evidence for tectonic escape in SW Taiwan. Tectonophysics 333:323–345

Lallemand SE, Liu CS, ACT cruise scientific team (1997) Swath bathymetry reveals active arc-continent collision near Taiwan. EOS. Trans Am Geophys Union 78:173–175

Li Q, Jian Z, Li B (2004) Oligocene–Miocene planktonic foraminifer biostratigraphy, Site 1148, northern South China Sea. In: Prell WL, Wang P, Blum P, Rea DK, Clemens SC (eds) Proceedings of ODP, Sci Results 184:pp 1–26

Lin AT, Watts AB, Hesselbo SP (2003) Cenozoic stratigraphy and subsidence history of the South China Sea margin in the Taiwan region. Basin Res 15(4):453–478

Lin AT, Liu CS, Lin CC, Schnurle P, Chen GY, Liao WZ, Teng LS, Chuang HJ, Wu MS (2008) Tectonic features associated with the overriding of an accretionary wedge on top of a rifted continental margin: an example from Taiwan. Mar Geol 255:186–203

Lin AT, Yao B, Hsu SK, Liu CS, Huang CY (2009a) Tectonic features of the incipient arc-continent collision zone of Taiwan: implications for seismicity. Tectonophysics 479:28–42

Lin CC, Lin AT, Liu CS, Chen GY, Liao WZ, Schnurle P (2009b) Geological controls on BSR occurrences in the incipient arc-continent collision zone off southwest Taiwan. Mar Petrol Geol 26:1118–1131

Liu CS, Huang IL, Teng LS (1997) Structural features off southwestern Taiwan. Mar Geol 137:305–319

Liu CS, Liu SY, Lallemand S, Lundberg N, Reed DL (1998) Digital elevation model offshore Taiwan and its tectonic implication. Terr Atmos Ocean Sci 9:705–738

Liu CS, Deffontaines B, Lu CY, Lallemand S (2004a) Deformation patterns of an accretionary wedge in the transition zone from subduction to collision offshore southwestern Taiwan. Mar Geophys Res 25:123–137

Liu JP, Milliman JD, Gao S, Cheng P (2004b) Holocene development of the Yellow River's subaqueous delta, North Yellow Sea. Mar Geol 209:45–67

Liu CS, Schnurle P, Wang Y, Chuang SH, Chen SC, Hsiuan TH (2006) Distribution and characters of gas hydrate offshore of southwestern Taiwan. Terr Atmos Ocean Sci 17:615–644

Løseth H, Gading M, Wensaas L (2009) Hydrocarbon leakage interpreted on seismic data. Mar Petrol Geol 26:1304–1319

Lowe JJ, Ammann B, Birks HH, Björck S, Coope GR, Cwynar L, deBeaulieu JL, Mott RJ, Peteet DM, Walker MJC (1994) Climatic changes in areas adjacent to the North Atlantic during the last glacial-interglacial transition (14–9 ka BP): a contribution to IGCP-253. J Quat Sci 9(2):185–198

Martinson DG, Pisias NG, Hays JD, Imbrie J, Moore TC, Shackleton NJ (1987) Age dating and the orbital theory of the ice ages: development of a high-resolution 0 to 300,000-year chronostratigraphy. Quat Res 27:1–29

Minshull T, White R (1989) Sediment compaction and fluid migration in the Makran accretionary prism. J Geophys Res 94:7387–7402

Mitchell NC (2006) Morphologies of knickpoints in submarine canyons. Geol Soc Am Bull 118:589–605

Moore GF, Taira A, Klaus A, Becker L, Boeckel B, Cragg BA, Dean A, Fergusson CL, Henry P, Hirano S, Hisamitsu T, Hunze S, Kastner M, Maltman AJ, Morgan JK, Murakami Y, Saffer DM, Sanchez-Gomez M, Screaton EJ, Smith DC, Spivack AJ, Steurer J, Tobin HJ, Ujiie K, Underwood MB, Wilson M (2001) New insights into deformation and fluid flow processes in the Nankai Trough accretionary prism: results of Ocean Drilling Program Leg 190. Geoch Geophs Geosystem 2:10.129/2001GC000166

Mosher DC (2011) A margin-wide BSR gas hydrate assessment: Canada's Atlantic margin. Mar Petrol Geol 28:1540–1553

Mouchot N, Loncke L, Mahieux G, Bourget J, Lallemant S, Ellouz-Zimmermann N, Leturmy P (2010) Recent sedimentary processes along the Makran trench (Makran active margin, off Pakistan). Mar Geol 271:17–31

Pirmez C, Beauboeuf RT, Friedmann SJ, Mohrig DC (2000) Equilibrium profile and baselevel in submarine channels: examples from Late Pleistocene systems and implications for the architecture of deepwater reservoirs. In: Weimer P, Slatt RM, Coleman J, Rosen NC, Nelson H, Bouma AH, Styzen MJ, Lawrence DT (eds) Deep water reservoirs of the world. GCSSEPM Foundation, Houston, pp 782–805

Reed DL, Lundberg N, Liu CS, Kuo BY (1992) Structural relations along the margins of the offshore Taiwan accretionary wedge: implication for accretion and crustal kinematics. Acta Geol Taiwan 30:105–122

Reilly JM (1993) Integration of well and seismic data for 3D velocity model building. First Break 11:247–260

Shipley TH, Houston MH, Buller RT, Shaub FJ, McMillen KJ, Ladd JW, Worzel JL (1979) Seismic reflection evidence for widespread occurrence of possible gas-hydrate horizons on continental slopes and rises. AAPG Bull 63:2204–2213

Shipley TH, Moore GF, Bangs NL, Moore JC, Stoffa PL (1994) Seismically inferred dilatancy distribution, northern Barbados Ridge decollement: implications for fluid migration and fault strength. Geology 22:411–414

Sibuet JC, Hsu S-K, Le Pichon X, Le Formal J-P, Reed D, Moore G, Liu CS (2002) East Asia plate tectonics since 15 Ma: constraints from the Taiwan region. Tectonophysics 344:103–134

Simoes M, Avouac JP, Chen YG, Singhvi AK, Wang CY, Jaiswal M, Chan YC, Bernard S (2007) Kinematic analysis of the Pakuashan fault tip fold, west central Taiwan: Shortening rate and age of folding inception. J Geophys Res 112(B03S14): 1–30

Smallwood (2002) Use of V_0-K depth conversion from shelf to deep-water: how deep is that bright spot? First Break 20: 99–107

Tobin HJ, Saffer DM (2009) Elevated fluid pressure and extreme mechanical weakness of a plate boundary thrust, Nankai Trough subduction zone. Geology 37:679–682

Turney CSM, Harkness DD, Lowe JJ (1998) Carbon isotope variations and chronology of the last glacial-interglacial transition (14–9 ka BP). Radiocarbon 40(2):873–881

Wang Y, Liu CS, the Taiwan gas hydrate research team (2009) Gas hydrate investigation in Taiwan. Fire in the ice winter 2009: 15–17

Wu S, Wang X, Wong HK, Zhang G (2007) Low-amplitude BSRs and gas hydrate concentration on the northern margin of the South China Sea. Mar Geophys Res 28:127–138

Yang KM, Wu JC, Ting HH, Wang JB, Chi WR, Kuo LC (1994) Sequential deformation in foothills belt, Hsinchu and Miaoli areas: implications in hydrocarbon accumulation. Petrol Geol Taiwan 29:47–74

Yu HS, Chang JF (2002) The Penghu submarine canyon off southwestern Taiwan: morphology and origin. Terr Atmos Ocean Sci 13:547–562

Yu HS, Hong E (2006) Shifting submarine canyons and development of a foreland basin in SW Taiwan: controls of foreland sedimentation and longitudinal sediment transport. J Asian Earth Sci 27:922–932

Yuan T, Hyndman RD, Spence GD, Desmons B (1996) Seismic velocity increase and deep-sea gas hydrate concentration above a bottom-simulating reflector on the northern Cascadia continental slope. J Geophys Res 101:13655–13671